Measurement 256 (2025) 118104

Contents lists available at ScienceDirect

Measurement

journal homepage: www.elsevier.com/locate/measurement

3D tomographic reconstruction of light emission density of plasma in the PROTO-SPHERA experiment

Annamaria Pau [a,*], Shayesteh Naghinajad [a], Franco Alladio [b], Paolo Micozzi [c], Luca Boncagni [c]

[a] Department of Structural and Geotchnical Engineering, Sapienza University of Rome, via Eudossiana 18, 00184 Roma, Italy
[b] INAF-IAPS National Institute of Astrophysics, Via del Fosso del Cavaliere 100, 00133 Roma, Italy
[c] Nuclear Research Department, ENEA Italian National Agency for Technology, Energy and Sustainable Economic Development, Via Enrico Fermi 45, 00044 Frascati (RM), Italy

ARTICLE INFO

Keywords:
3D image reconstruction
Magnetically confined plasma
Nuclear fusion
Monitoring

ABSTRACT

We address a key challenge in plasma diagnostics: reconstructing the three-dimensional (3D) light emission density from projection data. To this end, we employ a method for reconstructing 3D density functions based on a corollary of the 3D Fourier slice theorem. This corollary establishes a connection between 2D plane projections and plane sections of the 3D Fourier transform, enabling a direct and non-iterative solution to the inverse problem. The method is applied to the PROTO-SPHERA experiment, an innovative magnetic confinement plasma setup for controlled nuclear fusion research. Experimental data were acquired using six high-speed cameras arranged with cylindrical symmetry around the plasma chamber, capturing time-resolved pictures that are assumed to be parallel projections of the visible light emissions from Helium and Hydrogen discharges. After a transformation of coordinates, by computing their inverse 3D Fourier transform, we reconstruct the spatial distribution of light emission density. This technique enabled to reveal dynamic features of plasma self-organization — such as torus formation around a centerpost — and provides internal cross-sectional views of the plasma, displaying previously obscured spectral components.

1. Introduction

Tomographic computed (CT) imaging or scanning is a technique of data treatment which enables visualization of the inner part of objects instead of making real cuts. This has obvious and important applications in the medical field, as well as in the nondestructive monitoring of structures and industrial processes. CT requires the solution of an inverse problem, which can be formulated as follows: given the knowledge of some data called projections, reconstruct the spatial distribution of a density function $f(x, y, x)$ which represents some property (for instance mass density) of an object in the 3D space. Projections are obtained by illuminating the object with stimuli which produce a measurable response, which is measured on the object boundary. Projections are, in practice, a sort of shade that the function $f(x, y, x)$ projects onto lines, or planes. The mathematical demonstration that a density function could be reproduced from an infinite set of its projections was provided by the mathematician J. Radon [1] at the beginning of last century. However, it is quite remarkable that reconstruction of images from projections was not attempted until 1940. In 1972, Hounsfield [2] proposed the first method that allowed to image plane slices of the internal structure of a human body using X-rays projections. The Nobel prize in physiology and medicine in 1979 awarded to Hounsfield and Cormack [3] for their work on the initial computed tomography device signifies the importance that this technique has in the medical field. Since then, the use of computed tomography was extended to a wide number of industrial applications [4], among which food industry [5], materials science [6], geosciences [7] and fusion diagnostics [8–11].

Medical and industrial computed tomography is based on the same underlying principles but differs in the acquisition system layout, as well as in the stimulus that is used to obtain the projections, which is X-rays in medical CT, but can also be another physical source. In fact, the reflected or transmitted signal of any source which produces a measurable response of the scanned object can be used. The feasibility of using ultrasounds [12–14], the photo elastic effect [15], or even ground-penetrating radar emitting microwaves [16] has been proved to be effective to visualize internal patterns of objects. Different

* Corresponding author.
E-mail addresses: annamaria.pau@uniroma1.it (A. Pau), shayesteh.naghinajad94@gmail.com (S. Naghinajad), franco.alladio@protosphera.it (F. Alladio), paolo.micozzi@enea.it (P. Micozzi), luca.boncagni@enea.it (L. Boncagni).

https://doi.org/10.1016/j.measurement.2025.118104
Received 10 November 2024; Received in revised form 4 June 2025; Accepted 5 June 2025
Available online 20 June 2025

sources interact with different properties, which can include, besides mass density, electrical, acoustic, and electromagnetic properties of materials and tissues. For instance, in nuclear medicine, the interest is focused on reconstructing a cross-sectional image of radioactive isotope distributions within the human body [17], while in magnetic resonance the magnetic properties of the object is reconstructed [18]. The photoelastic effect instead was used to determine the plane stress distribution in an optical fiber [19]. The most fundamental distinction between medical CT and fusion diagnostics lies in the nature of the signal: while medical tomography is primarily concerned with absorption, fusion diagnostics focuses on emission. The main difference between the mentioned sources is that some of them are non-diffracting, like X-rays, which travel in straight lines [20], while some others are diffracting, like ultrasounds, that is, they are scattered in all directions, resulting in a more complex inverse problem [21].

To convert the measured response data into an image, appropriate processing is necessary. The most popular algorithms that are in use can be classified into two major categories, which are iterative and analytical methods [22]. Iterative methods are numerical reconstruction algorithms that employ a model to predict the measured data from an initial estimate and then refine the image estimate to better fit the measured data. This process is repeated iteratively until the image quality meets a predetermined standard or until further iterations do not significantly change the image [23,24]. Starting from the Algebraic Reconstruction Technique (ART) [25], research continues to evolve with refinements and developments, such as the customized Simultaneous Algebraic Reconstruction Technique (SART) [26], and the Simultaneous Iterative Reconstruction Technique (SIRT) [27]. Analytical algorithms are based on mathematical models and explicit formulas that directly compute the image from the acquired projection data. They can be further categorized into two groups: the direct or Fourier-Transform-based methods [28,29] and the Back-Projection-based algorithms, like Simple Back Projection (SBP), Linear Back Projection (LBP) and Filtered Back Projection (FBP) [27,30]. Fourier-Transform-based algorithms rely on the relationship between the Fourier transform (FT) of the image and the Fourier transform of its projections. More specifically, projections are obtained using Radon transforms [21], that is by computing line integrals of the density function. A more detailed discussion of the literature on the classification of CT algorithms is beyond the scope of this paper. The interested reader can consult [14,31] for a more exhaustive presentation of the matter.

2. Application of tomography to fusion diagnostics

In tokamaks, reconstruction of X-ray emission relies on data collected by line-integrated detectors — such as pinhole X-ray cameras, bolometers, and neutron cameras — arranged across a cross-section of the plasma. Unlike medical imaging systems, which benefit from unrestricted access to the subject from all angles, fusion diagnostics is constrained by the geometry of the tokamak. The number and placement of detectors are limited by the physical design of the device, leading to a much lower spatial resolution than that achievable in medical tomography. As a consequence of this sparse and uneven data, plasma tomography requires additional assumptions, such as smoothness or regularity of the emission field, regardless of the inversion technique employed [32].

Under these circumstances, analytical and iterative methods faced various challenges, prompting the development of dedicated numerical techniques specifically tailored for 2D cross-sectional plasma tomography. These numerical approaches rely on an algebraic formulation of the image reconstruction problem, where each equation represents the equality between a known measured integral and the sum of emissions along a corresponding line of sight. However, the resulting system is typically underdetermined and the problem ill-posed, with high sensitivity to data error. To address this issue, various regularization techniques are employed to constrain the solution space, often by promoting smoothness or limiting complexity in the results. Among the robust regularization methods used in plasma tomography, Tikhonov regularization, Maximum Likelihood estimation, and Fisher information-based approaches are particularly noteworthy [10,11]. In addition, there have been efforts to apply neural networks and deep learning techniques to tomographic reconstruction, offering promising alternatives for handling the inherent challenges of the problem [9].

In this work, we aim to apply tomographic techniques to reconstruct the light emission density recorded during the PROTO-SPHERA experiment deployment [33], conducted at the ENEA laboratories (Italian National Agency for New Technologies, Energy and Sustainable Development) in Frascati, Italy. During the experiment, the plasma emits photons, whose light is captured by six cameras arranged with cylindrical symmetry. PROTO-SPHERA is an innovative magnetic confinement plasma experiment designed for research in controlled thermonuclear fusion. Its goal is to form a plasma torus not around a solid metal centerpost, as in traditional tokamaks, but around a plasma centerpost. This setup introduces significant differences compared to the reconstruction of X-ray emission density in tokamaks. Firstly, PROTO-SPHERA provides unobstructed visual access from any viewing angle. Secondly, the plasma produced by PROTO-SPHERA has emission concentrated in the visible and ultraviolet spectrum. Last but not least, the optical system uses lenses, producing a sharp image with limited perspective effect, due to the distance between plasma and cameras. The image can then be treated as a parallel projection of light emission.

To the best of our knowledge, fusion plasma tomography was only carried out on sections of the torus. Here, we employ the imaging technique based on a corollary to Fourier slice theorem in 3D, also called Fourier Section Theorem [34,35] and based on an nth-dimension formulation of the Radon transform, provided by Radon himself: by calculating 3D inverse Fourier transforms of 2D Fourier transforms of plane projections, the 3D image of the scanned object can be reconstructed. This differs from the classical tomographic approach [36,37], where a 3D image is reconstructed by assembling stacks of images deriving from reconstructed images on several parallel planes. This work represents a first step toward 3D reconstruction of the plasma visible light emission density, which has never been attempted before. The resulting images enabled the observation of important aspects of plasma formation and arrangement.

This paper is organized into two sections: Section 3 revises the method of image reconstruction in 3D based on a corollary of the Fourier slice theorem, and Section 4 reports the experimental results. For the ease of the reader, in Section 3.1, the 3D continuous Radon transform is recalled, then in Section 3.2 the lemma of the Fourier slice theorem that is at the base of the image reconstruction method employed is presented. In Section 3.3 proof of the effectiveness of the reconstruction method is provided by using numerical data. Section 4.1 describes the PROTO-SPHERA experiments, and Section 4.2 illustrates how the tomographic reconstruction enabled to prove the sustainment of the plasma torus around the centerpost and provided further useful information on the dynamics of confined plasma.

3. Analytical direct 3D image reconstruction

3.1. 3D continuous Radon transform

For simplicity's sake, the 2D Radon transform is first introduced. Let us consider a plane object — or a slice of a 3D object — with density function $f(x, y)$ (Fig. 1). Its projections onto a line inclined by an angle θ with respect to the x axis are obtained by integrating $f(x, y)$ on the set of parallel lines (rays) that are inclined by an angle $\theta+\pi/2$ with respect to the x axis and at a distance t from the origin of the coordinate system (bold line in Fig. 1). The equation of a ray is:

$$t = x\,cos\theta + y\,sin\theta. \tag{1}$$

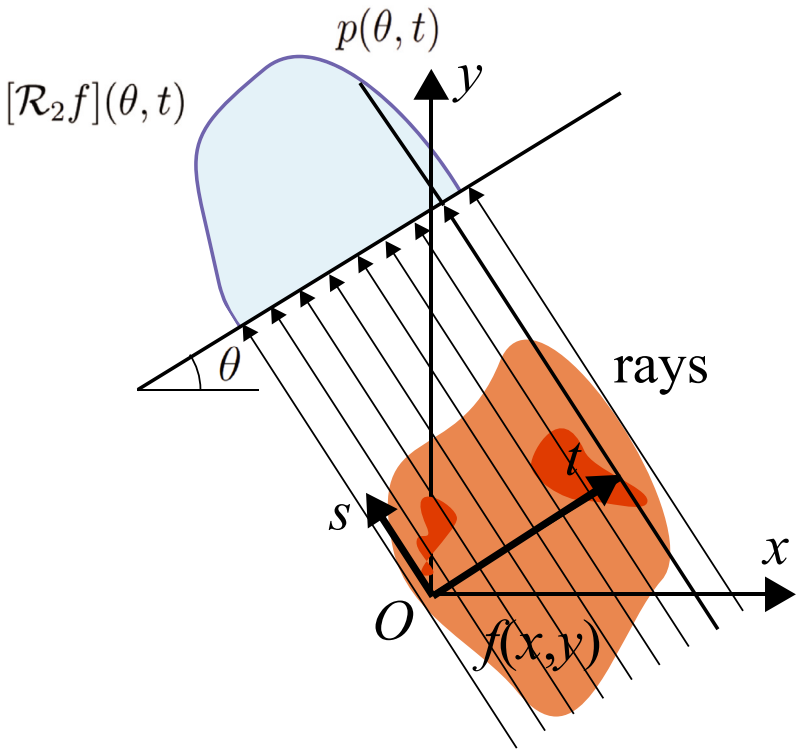

Fig. 1. Projection of a plane density function onto a line.

The projection of the function $f(x,y)$ is then defined as:

$$p(\theta,t) = \int_{-\infty}^{\infty}\int_{-\infty}^{\infty} f(x,y)\delta(x\,cos\theta + y\,sin\theta - t)dxdy, \tag{2}$$

where δ is the Dirac's delta function. Eq. (2) represents the 2D continuous Radon transform $[\mathcal{R}_2 f](\theta,t)$ of the function f, which is depicted schematically in Fig. 1 by the blue curve subtending the sky blue area. It is often preferred to integrate in the rotated coordinate system (t,s), where the projection can be written as:

$$p(\theta,t) = \int_{-\infty}^{\infty} f(t,s)ds. \tag{3}$$

Geometrically, the continuous 2D Radon transform maps a function in $\mathbb{R}^2$ into the set of its line integrals in $\mathbb{R}^2$. The reconstructed image function $f(x,y)$ is formally obtained by inverting the Radon transform:

$$f(x,y) = [\mathcal{R}_2^{-1} p](\theta,t). \tag{4}$$

Let us now consider a 3D object with density function $f(x,y,z)$ (Fig. 2). Its projections are obtained by integrating $f(x,y,z)$ on the plane Σ that is orthogonal to the versor $\boldsymbol{\alpha}$ and at a distance d from the origin of the coordinate system. The versor has direction cosines $\boldsymbol{\alpha} = (cos\theta\,cos\phi, sin\theta\,cos\phi, sin\,\phi)^T$, where ϕ is the angle that $\boldsymbol{\alpha}$ forms with the z axis, and θ is the angle that the projection of $\boldsymbol{\alpha}$ onto the xy plane forms with the x axis. The equation of a plane orthogonal to $\boldsymbol{\alpha}$ and at a distance d from the origin is:

$$d = x\,cos\theta\,cos\phi + y\,sin\theta\,cos\phi + z\,sin\phi. \tag{5}$$

In an analogy with Eq. (2), the projection of the function $f(x,y,z)$ associated with the couple $(\boldsymbol{\alpha},d)$ is then defined as:

$$p(\boldsymbol{\alpha},d) = \int_{-\infty}^{\infty}\int_{-\infty}^{\infty}\int_{-\infty}^{\infty} f(x,y,z)\delta(x\,cos\theta\,cos\phi + y\,cos\theta\,sin\phi + z\,sin\theta - d)dxdydz. \tag{6}$$

The area over which the previous integral is computed is included in the dashed line in Fig. 2. Eq. (6) represents the 3D continuous Radon transform $[\mathcal{R}_3 f](\boldsymbol{\alpha},t)$ of the function f. Geometrically, the continuous 3D Radon transform maps a function in $\mathbb{R}^3$ into the set of its plane integrals in $\mathbb{R}^3$. The reconstructed image function $f(x,y,z)$ is formally obtained by inverting the Radon transform:

$$f(x,y,z) = [\mathcal{R}_3^{-1} p](\boldsymbol{\alpha},d). \tag{7}$$

It is important to note that in real applications we won't be dealing with plane integrals. In fact, $\mathcal{R}_3$ can be obtained by computing the $\mathcal{R}_2$ of the intersection between f and the plane Σ, and then integrating over lines orthogonal to the rays, which are displayed in Fig. 3 as yellow lines. The line integrals are much easier to be obtained in practical measurements. They correspond to projections onto detector planes taken from different angles, or, in the present case, to pictures taken from different cameras.

With the definition introduced above, the detector plane still has a rotational degree of freedom around the detector normal. Different from what is done in [34], here we integrate in the rotated coordinate system (t,s,r), whose axes t and s coincide with the tangent lines to the parallels and meridians, respectively, of an imaginary sphere centered in the origin of the system of coordinates, at the point of intersection between the sphere and the versor $\boldsymbol{\alpha}$, with the orientation of the r axis coinciding with that of $\boldsymbol{\alpha}$ (Fig. 3, upper left). The plane (t,s) is the detector plane. The transformation of coordinates from (x,y,z) to (t,s,r) can be written as:

$$\begin{bmatrix} t \\ s \\ r \end{bmatrix} = \begin{bmatrix} cos\phi & 0 & sin\phi \\ 0 & 1 & 0 \\ sin\phi & 0 & cos\phi \end{bmatrix} \begin{bmatrix} cos\theta & sin\theta & 0 \\ -sin\theta & cos\theta & 0 \\ 0 & 0 & 1 \end{bmatrix} \begin{bmatrix} x \\ y \\ z \end{bmatrix}. \tag{8}$$

Moreover, the distance d can be expressed in the (t,s,r) system of coordinates as $d = \sqrt{t^2 + r^2}$. The ray integral is then expressed as follows:

$$p(\theta,\phi,t,r) = \int_{-\infty}^{\infty} f(t,s,r)ds. \tag{9}$$

The integral $p(\theta,\phi,t,r)$ is in practice a line projection of the 3D function. The set of all the line projections on the plane (t,r) for given θ and ϕ will be denoted as $P_{\theta,\phi}$.

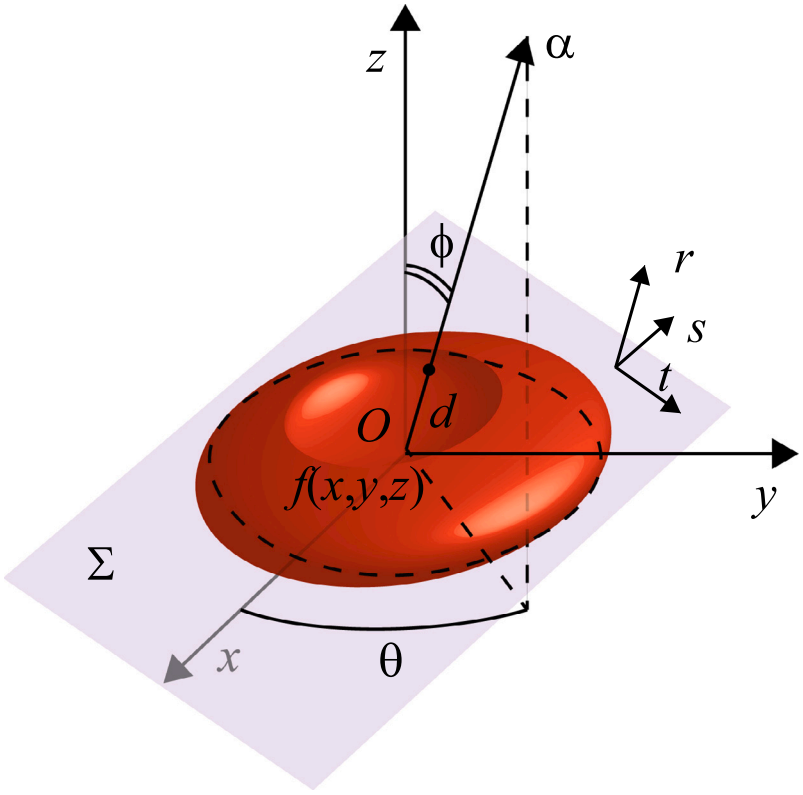

Fig. 2. Projection of a 3D density function onto a plane.

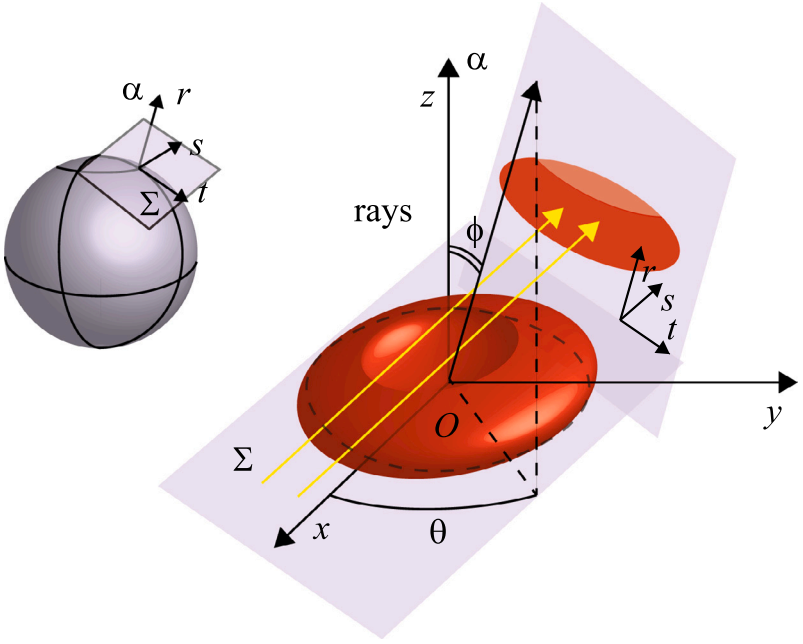

Fig. 3. Ray integrals over a 3D function.

3.2. 3D Fourier slice theorem

The extension of the Fourier slice theorem to higher dimensions, enables direct reconstruction of 3D objects. The 3D Fourier Slice Theorem can be stated as follows.

Theorem 1. *A line slice of the 3D Fourier transform of the function $f(x, y, z)$ equals the 1D Fourier Transform of the 3D Radon transform $[\mathcal{R}_3 f](\boldsymbol{\alpha}, t)$ at the same angle.*

For proof, the interested reader can consult [35,38]. However, the theorem in this form is of little use for practical purposes. A useful corollary can be stated. See for instance [34].

Corollary 1.1. *A plane slice of the 3D Fourier transform of the density function $f(x, y, z)$ equals the 2D Fourier Transform of the set of line projections at the same angle.*

Proof. Let us consider the line projection of a 3D density function $P_{\theta,\phi}$, and take its 2D Fourier Transform ($\mathcal{F}_2$):

$$[\mathcal{F}_2 P_{\theta,\phi}](\mu, \nu) = \int_{-\infty}^{\infty}\int_{-\infty}^{\infty} P_{\theta,\phi}(t, r) e^{-2\pi i(\mu t + \nu r)} dt dr, \tag{10}$$

where μ and ν are the wavenumbers in the t, r directions, respectively and i is the imaginary unit.

By substituting Eq. (9) into Eq. (10), we get:

$$[\mathcal{F}_2 P_{\theta,\phi}](\mu, \nu) = \int_{-\infty}^{\infty}\int_{-\infty}^{\infty}[\int_{-\infty}^{\infty} f(t, s, r) ds] e^{-2\pi i(\mu t + \nu r)} dt dr. \tag{11}$$

Based on the transformation (8), the rotated coordinate system (t, s, r) can be converted back into the initial (x, y, z) system:

$$[\mathcal{F}_2 P_{\theta,\phi}](\mu, \nu) = \int_{-\infty}^{\infty}\int_{-\infty}^{\infty}\int_{-\infty}^{\infty} f(x, y, z)\, e^{-2\pi i k}\, dx\, dy\, dz \tag{12}$$

$$\text{with} \quad k = \mu\cos\phi\cos\theta\, x + \mu\cos\phi\sin\theta\, y + \mu\sin\phi\, z + \nu\sin\phi\cos\theta\, x + \nu\sin\phi\sin\theta\, y + \nu\cos\phi\, z.$$

It is obvious that, with a transformation of coordinates, the right hand side of (12) represents the 3D Fourier Transform $\mathcal{F}_3$ of f at wavenumbers $u = \mu cos\phi cos\theta + \nu sin\phi cos\theta$, $v = \mu cos\phi sin\theta + \nu sin\phi sin\theta$ and $w = \mu sin\phi + \nu cos\phi$:

$$[\mathcal{F}_3 f](u, v, w) \int_{-\infty}^{\infty}\int_{-\infty}^{\infty}\int_{-\infty}^{\infty} f(x, y, z) e^{-2\pi i(ux+vy+wz)} dx dy dz, \tag{13}$$

which proves the corollary. The quantities u, v and w are wavenumbers in directions x, y and z, respectively. □

The interesting consequence of this corollary is that, given the plane projections, calculating their 2D Fourier Transform, and then computing the inverse 3D Fourier Transform of the resulting set of 2D Fourier transforms after a transformation of coordinates, the original image is directly reconstructed. Fig. 4 reports a flowchart of the described image reconstruction procedure. The following subsection provides numerical proof.

3.3. Numerical example of the 3D direct reconstruction

Let us consider an input density function modeled as a cube with a uniform density of 0.5, side length of 0.6, and centered at the origin of the coordinate system (Fig. 5a). Inside this cube, two smaller spheres are embedded: one with a density of 0.3, a radius of 0.1, and centered at coordinates (0.05, 0.05, −0.2); the other with a density of 0.1, a radius of 0.05, and centered at (−0.1, 0, 0.1). These variations in density are used to verify the accuracy of the reconstruction, ensuring it can effectively distinguish between different density regions. Although the spheres are not visible from the exterior of the solid cube, Fig. 5b illustrates their positions by rendering the cube with partial transparency. It is important to note that for this numerical example, the theoretical framework developed for continuous systems in the previous sections has been adapted for use with discrete data. In this case, we employed a total of $N = 64 \times 64 \times 64$ sampling points, with 64 points along each side of the cube. Additionally, $N_{deg} = 12{\times}12 = 144$ spherical projections were taken, with 12 projections for each angle θ and ϕ, respectively. The angular step size was kept constant over π, set to $\pi/12$.

Figs. 6a and b provide samples of the spherical projections used for reconstruction, taken at angles $(\theta, \phi) = (\pi/2, 0)$ and $(2\pi/3, 0)$, respectively. Note that the color scale extends beyond 0.5 because it represents line integrals of the density function over the entire domain, rather than local values. Regions of lower density show in fact lower integral values. At this point, it is necessary that 144 2D Fourier Transforms of the spherical projections are computed. These Transforms are defined on the plane (μ, ν) (Eq. (11)). However, computing the inverse 3D Fourier Transform requires knowledge of the data on a Cartesian grid of wavenumbers (u, v, w) (Eq. (12)). Therefore, after the transformation of coordinates, discrete data available has to be interpolated to obtain the values onto a regularly spaced Cartesian grid, then 3D inverted. In this way, the reconstructed density function shown in Fig. 7a is obtained, matching the original function from Fig. 5a. Figs. 7b, c, and d present cross-sections of the reconstructed density function along two vertical planes (b,c) and a horizontal plane (d) passing through the origin, with the corresponding color scale. This Figure shows that the embedded spheres are exactly reconstructed not only in terms of position, but also in terms of density. See in fact that the large sphere has high density, while the small one low.

The previous example was implemented using a large number of projections. While reducing the number of projections results in a slightly blurred reconstructed image, even a very limited number of projections still provides a sufficiently clear reconstruction. This effect is illustrated in Fig. 8, which shows the reconstructed density function with varying numbers of projections. The source density function is depicted in Fig. 8(a). It is shaped as a cube with a unit density, a side length of 0.2, and is centered at the origin of the coordinate system. A sphere with unit density, a diameter larger than the cube's side, and centered at the origin, was subtracted from the density function, causing its volume to intersect with the cube's faces. Although the image quality decreases as the number of projections is reduced, the shape remains distinctly recognizable even with a very limited number of projections, as few as 9 (Fig. 8d).

4. 3D reconstruction of light emission density in PROTO-SPHERA experiment

4.1. The PROTO-SPHERA experiment

PROTO-SPHERA (Spherical Plasma for HElicity Relaxation Assessment) is an innovative magnetic confinement plasma experiment aimed at advancing controlled thermonuclear fusion research. Its goal is to form plasma within a confined environment. Unlike tokamaks, where the plasma forms around a metal centerpost, in PROTO-SPHERA, the plasma forms around a plasma centerpost [39–41]. Tokamaks, the most extensively studied magnetic fusion configurations, have a non-simply connected geometry, where a central post—containing the inner part of the toroidal magnet and the ohmic transformer—connects the plasma torus. The development of simply connected magnetic configurations relevant for fusion would significantly simplify the design of fusion reactors. Additionally, the PROTO-SPHERA experiment seeks to emulate astrophysical plasmas, such as jet and torus structures, in a laboratory setting [33].

Fig. 9 shows a schematic of the PROTO-SPHERA experiment, which consists of a transparent cylindrical vacuum chamber measuring 2.5 meters in height and 2.0 meters in diameter, held by a metal structure (Fig. 9a). The vacuum chamber, surrounded by four columns, is equipped with electrodes at its ends and internal poloidal field coils (Fig. 9b). The operating sequence proceeds as follows: the tungsten

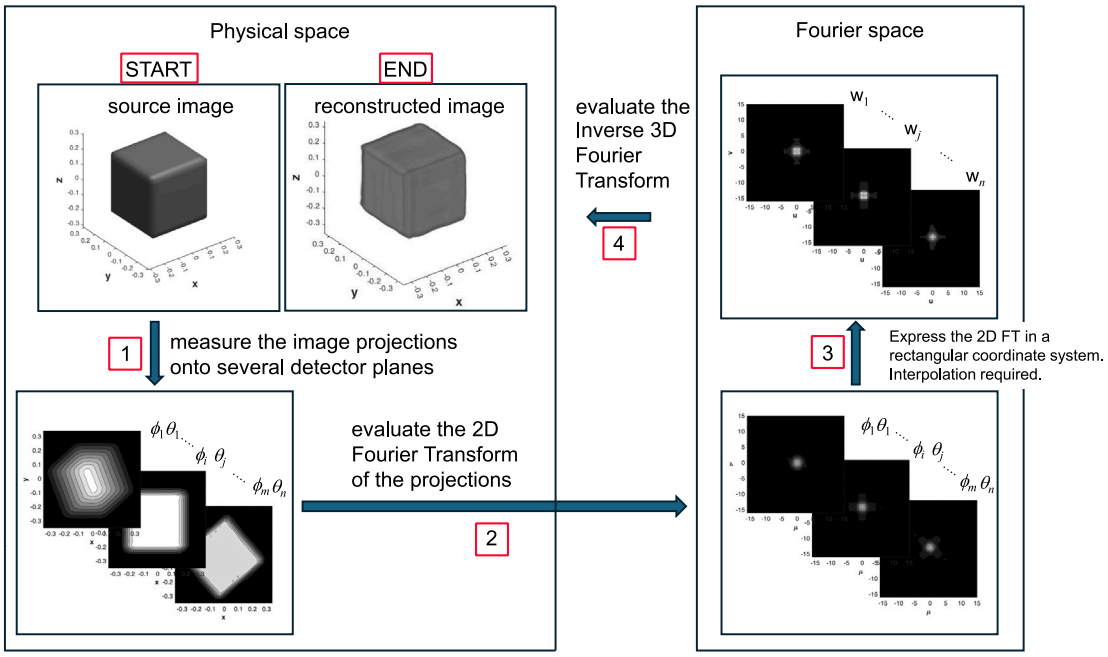

Fig. 4. Flowchart of the image reconstruction procedure.

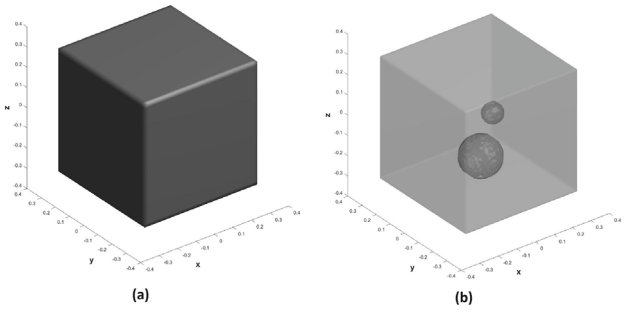

Fig. 5. (a) 3D density function (b) density function made partially transparent to show the embedded spheres.

filaments of the cathode are heated to 2600–2900 °C over 30 s, while the current in the poloidal field coils is ramped up to its final value. Gas is then introduced through a hollow section in the anode, reaching a pressure of 10^{-2} to 10^{-1} mbar, and a total voltage of 100–350 V is applied between the electrodes, yielding a centerpost current up to 10 kAmp. Under these conditions, cold plasma with an energy in the range of 20–30 eV forms, with an emission concentrated in the visible and ultraviolet spectrum.

To study the plasma formation process and the magneto-hydrodynamic phenomena occurring in the experiment, six high-speed cameras are positioned on the equatorial plane of the chamber, spaced 60 degrees apart (Fig. 10). It should be noted that in an ideal scenario free from errors, two cameras placed exactly 180 degrees apart would provide redundant information. However, real-world measurements are inevitably affected by several sources of error. These include, but are not limited to, slight misalignments in camera positioning, optical distortions, slight differences in vignetting due to material objects present inside the vessel, thermal expansion, structural vibrations, and electronic noise. In this context, having views from opposite sides of the plasma increases the robustness of the reconstruction and helps mitigate the effects of such errors. Each camera has a resolution of 640 × 480 pixels and can capture 600 frames per second. Sample images recorded by the cameras at a specific time instant are shown in Figs. 11a and 12a for shots with Helium and Hydrogen, respectively.

Combining the data from the cameras with measurements from a Langmuir probe has provided valuable insights into the dynamics of the plasma torus formation, including its size and emission spectrum. Numerous discharges were produced and observed throughout the experimental campaign.

The images captured by the six cameras are assumed to be parallel projections onto vertical planes corresponding to the camera views of the visible-light emission density, which plays the role of the density function f (Figs. 11a and 12a). For each time instant, exploiting the corollary of the Fourier Slice Theorem of Section 3, these source images are 2D-Fourier transformed, then 3D-Fourier inverted to obtain the density of the visible light emitted by the plasma. The only change with respect to the procedure described in Section 3.2 is that, given the positioning of the cameras, the inversion has to be based on a cylindrical set of parallel projections instead of a spherical set, with ϕ fixed. Figs. 11b and 12b show the reconstructed plasma light emission distribution derived from the images on the left for Helium and Hydrogen, respectively. It is important to note that the original images contain three layers of information, corresponding to the RGB color channels. The reconstructed images in Figs. 11b and 12b are false-color representations, created by combining the RGB channels linearly with the following weighting: 100% Red, 86% Green, and 25% Blue [33].

4.2. Results and discussion

The proposed 3D tomography technique enabled detailed observation of the plasma torus formation process. The sequence begins with the formation of a plasma column (pinch or centerpost) at a current lower than 10 kAmps. As the current reaches this value, the magnetic field lines bend, causing the pinch to become unstable, which leads to the formation of a torus around the centerpost. This progression is visualized in Fig. 13 a–h, showing the reconstructed light emission density at eight sequential time steps (each 1/600 s apart) during a Helium plasma discharge. These findings align closely with predictions from magnetohydrodynamic (MHD) models, in particular those presented in the work by García-Martínez et al. [42], whose magnetic field lines at different Lundquist numbers present a striking topological similarity

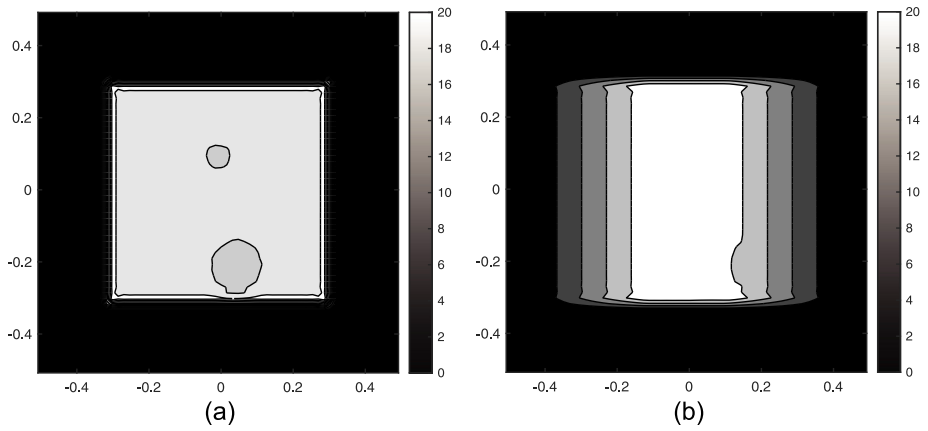

Fig. 6. A couple of spherical projections pertaining to angles (a) $\theta = \pi/2$, $\phi = 0$ and (b) $\theta = 2\pi/3$, $\phi = 0$.

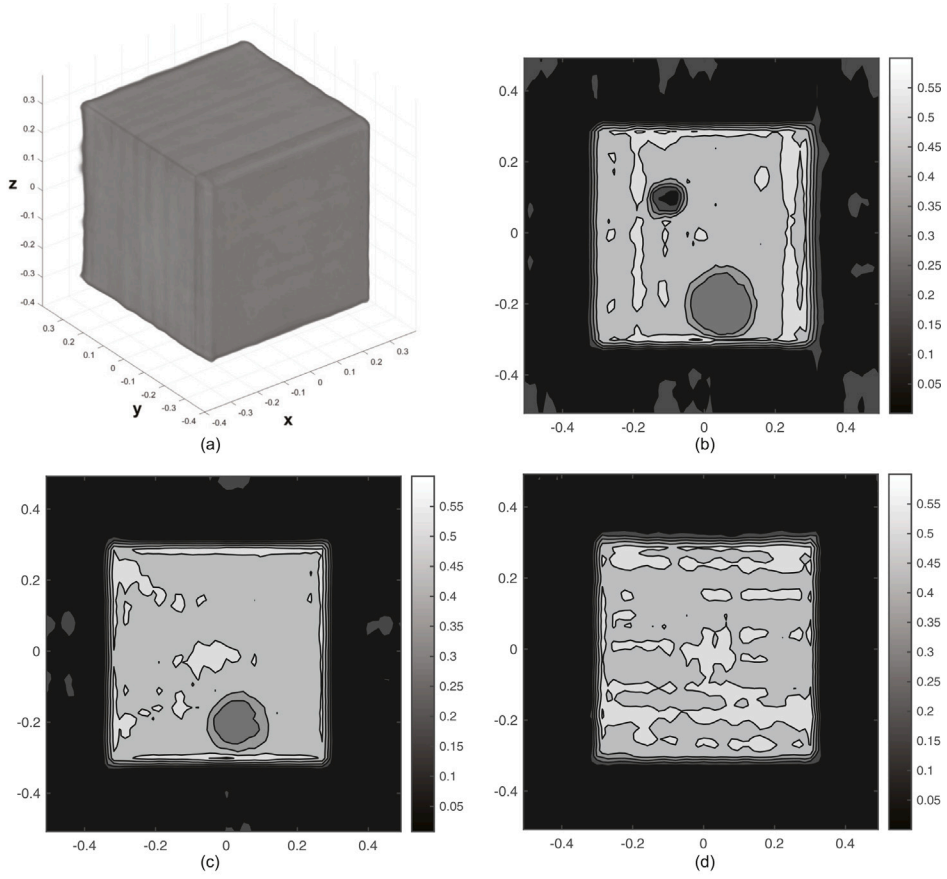

Fig. 7. (a) Reconstructed image, (b) vertical cross section on the xz plane, (c) vertical cross section on the yz plane, (d) horizontal cross section on the xy plane.

with our emission density reconstruction (see Figure of 8 [42]). The entire torus formation occurs within approximately 8 ms, five time steps intercurring from the arrangements of Fig. 13 b to g. The presence of both jets and the torus strongly parallels astrophysical phenomena, as discussed in [33].

Once the spatial distribution of light emission density is known for each time instant, cross-sections can be derived, revealing further insights into plasma dynamics. Fig. 14 shows an image of the Helium plasma captured by one of the six cameras (a) and a vertical cross-section (b) of the reconstructed light emission density in true color, taken at the same moment. To create this image, each of the three RGB channels was processed independently to generate a corresponding density function for each color. This cross-sectional view reveals the green color, which was obscured in the camera pictures by the intense orange glow of the 'ionization peel'—the layer between the plasma and the surrounding gas cushion. The correctness of the reconstruction is proved by the appearance of the Langmuir probe and of the copper bars on the right hand side of the picture. These are external conducting copper bars (3 cm in diameter) that connect the two electrodes.

Fig. 15 presents vertical cross-sections of the plasma light emission density at the same time instants as Fig. 13. These images further confirm the sequence of events leading to the formation of the torus, as described in the previous paragraph. Specifically, Fig. 15 illustrates the emergence of a stable pinch (a–b), its progression toward instability (c–f), and ultimately the arrangement of the torus around the

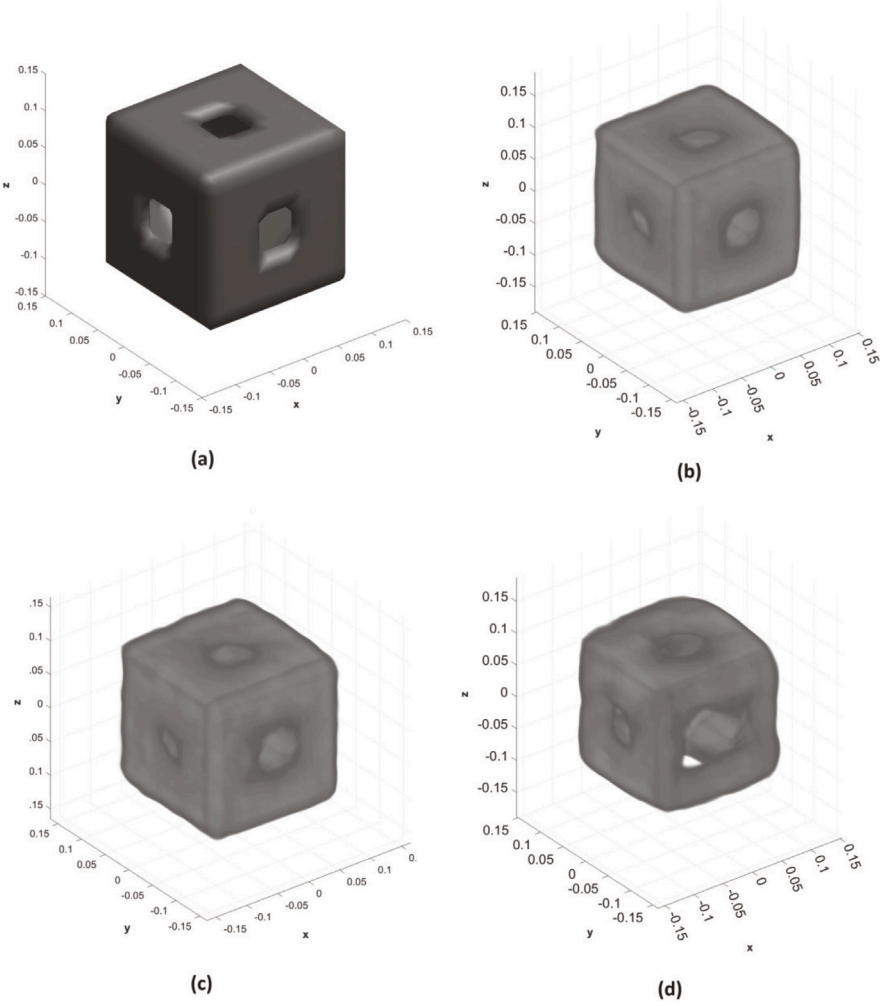

Fig. 8. (a) Source image and Reconstructed image with (b) 12×, (c) 6 × 6 and (d) 3 × 3 projections.

centerpost (d–h). Similar patterns, with comparable duration, were observed in other plasma discharges [33,43]. Fig. 16 presents a horizontal cross-section at the equatorial level, enabling observation of the same phenomena from a different perspective. In Figs. 16d and 16e, the pinch's instability is particularly evident, as shown by the loss of axial symmetry and the presence of green regions on the right side of the images. The phenomena described, featuring a centerpost around which a toroidal structure forms, show similar morphology with some theoretical results presented in [42], concerning MHD models, in particular, with those displaying the ratio between current density and magnetic field of an equatorial section. Further experimental confirmation of our finding comes from the PROTO-SPHERA research group, who obtained similar results using different reconstruction techniques. Specifically, Fig. 17 reproduces a Figure of the work [44], and displays the plasma luminosity obtained through tomographic inversion using Zernike polynomials. The data in this figure refers to earlier experiments conducted with Argon gas and are shown in false colors. Data support the presence of the toroidal light emission structure and of the centerpost observed in our study. In the experiments reported in [44] not all the details of the setup had been finalized.

Additionally, the horizontal cross-section analysis provides insights into plasma stability and torus thickness. Fig. 18 illustrates selected horizontal cross-sections of Helium plasma at the equatorial level across sequential times, clearly depicting the torus encircling the centerpost. Notably, the light emission intensity varies over time, suggesting potential correlations with plasma density and stability. These images also allowed for the measurement of torus thickness, defined as the difference between the outer and inner circumferences' radii, which was observed to be between 0.25 and 0.35 m. Note that, in Fig. 18, the angle brilliance visible at the four corners is likely due to the reflection of light from the four metal columns supporting the vessel. Similar behaviors were noted for Hydrogen plasma discharges, with an equatorial horizontal cross-section provided in Fig. 19 for reference.

5. Conclusions

An imaging technique based on a corollary of the Fourier slice theorem was applied to reconstruct the light emission distribution of magnetically confined plasma in three dimensions. The derived algorithm was used on pictures capturing the visible light emission from Helium and Hydrogen plasmas, recorded by six cameras as part of the PROTO-SPHERA experiment at the ENEA Frascati laboratories. The results demonstrate that six images taken by cameras arranged in cylindrical symmetry enable an accurate 3D reconstruction of the plasma's spatial light emission density distribution at different time instants during the experiment. We observed that the plasma torus forms in approximately 8 ms, evolving from a kinked filament caused by the destabilization of the plasma centerpost. This 3D reconstruction allows for cross-sectional analysis, revealing previously hidden green light emission from the core, which had been obscured by the outer orange ionized layer. Additionally, equatorial cross-sections enabled

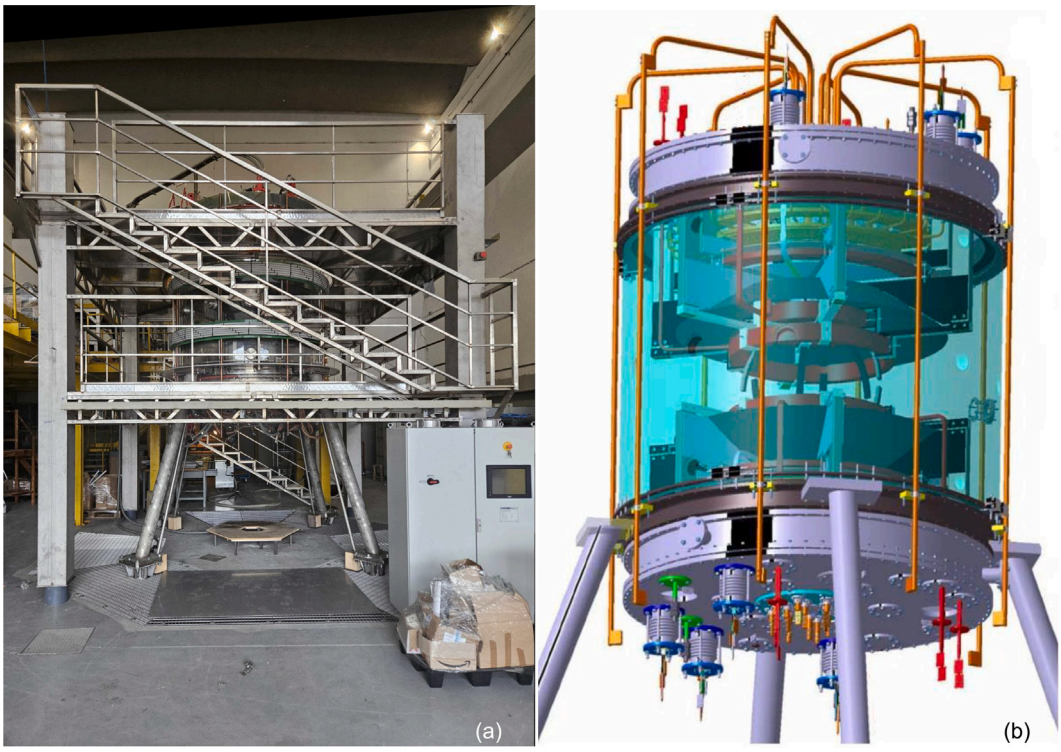

Fig. 9. (a) Picture of PROTO-SPHERA setup and (b) schematic of the machine.

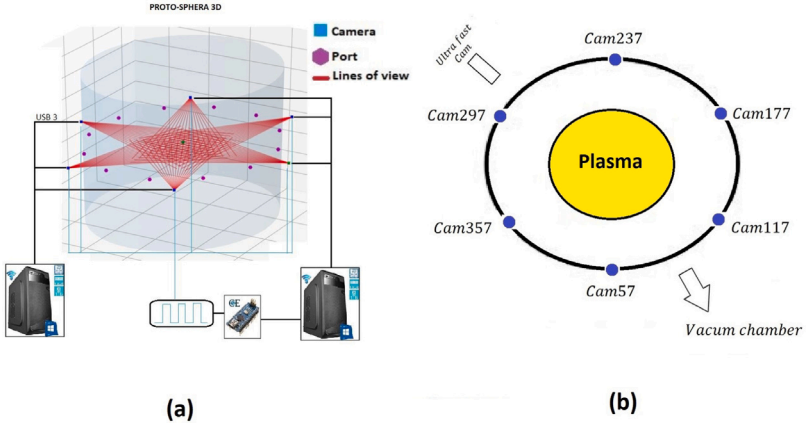

Fig. 10. (a) Position of the cameras in axonometry (b) and plan.

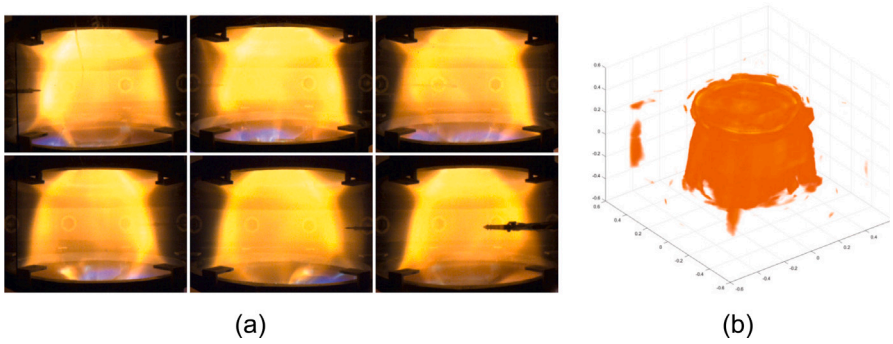

Fig. 11. (a) Pictures recorded by the six cameras at a given time instant (267 ms) of the PROTO-SPHERA experiment from shot 2505 of Helium (b) 3D reconstruction of plasma light emission density.

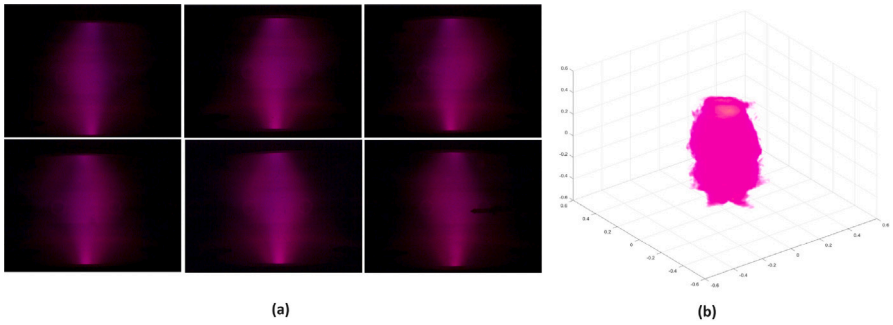

Fig. 12. (a) Pictures recorded by the six cameras at a given time instant (233 ms) of the PROTO-SPHERA experiment from shot 2154 of Hydrogen (b) 3D reconstruction of plasma light emission density.

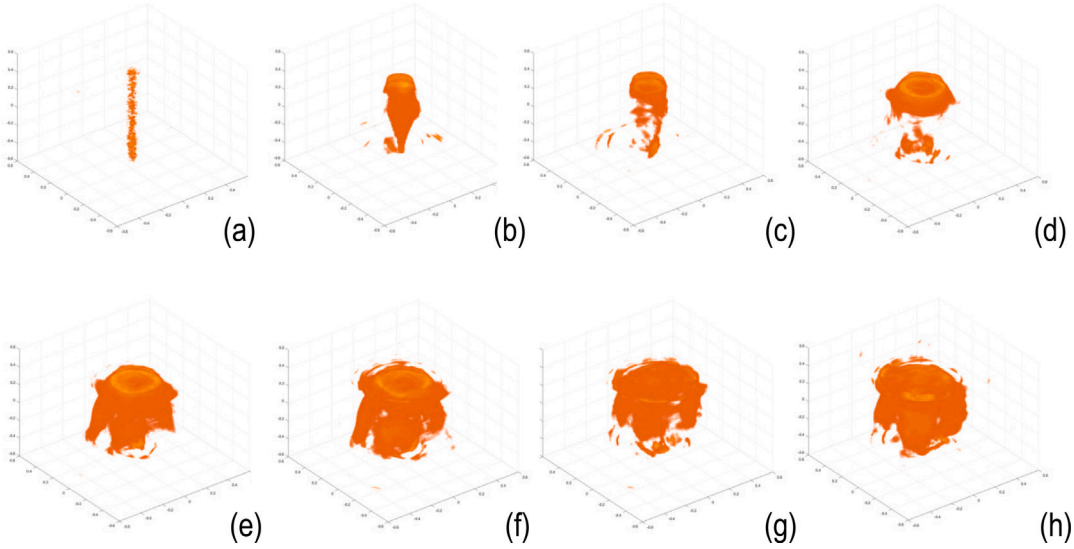

Fig. 13. Reconstructed light emission density of Helium discharge 2505 at eight sequential time steps: stable pinch (a–b), pinch instability (c–f), formation of the plasma torus around the pinch (g–h).

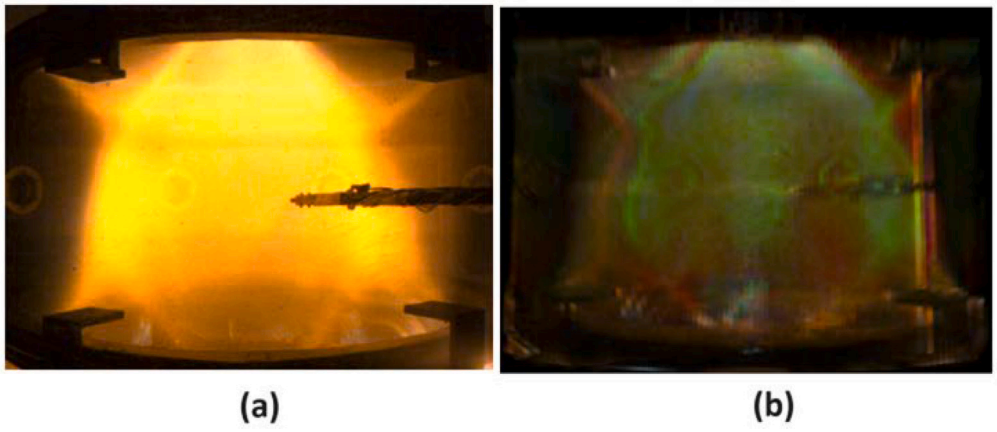

Fig. 14. A projection of Helium plasma visible light emission captured by a camera during shot 2141 (a) and cross-section of the reconstructed light emission density in true colors (b).

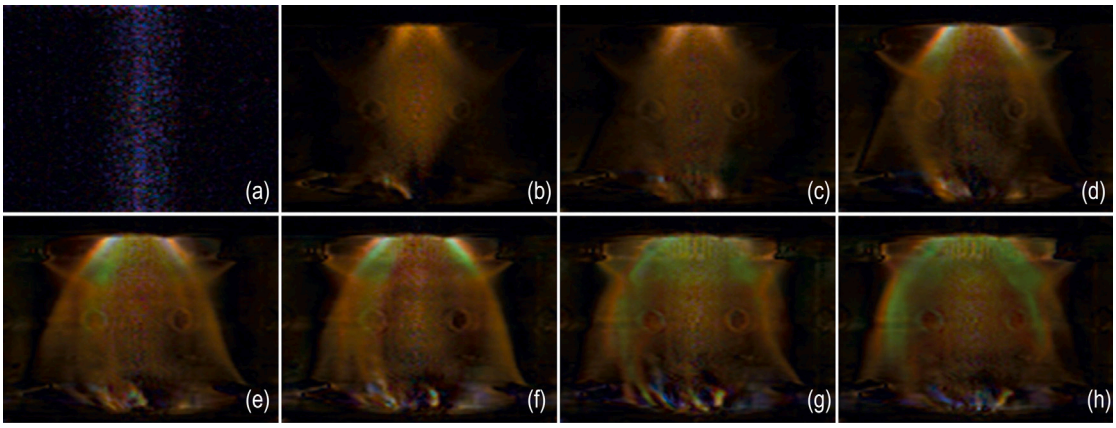

Fig. 15. Vertical cross-sections of the reconstructed light emission density of Helium discharge 2505 at the same eight sequential time instants as Fig. 12: stable pinch (a–b), pinch instability (c–f), formation of the plasma torus around the pinch (g–h).

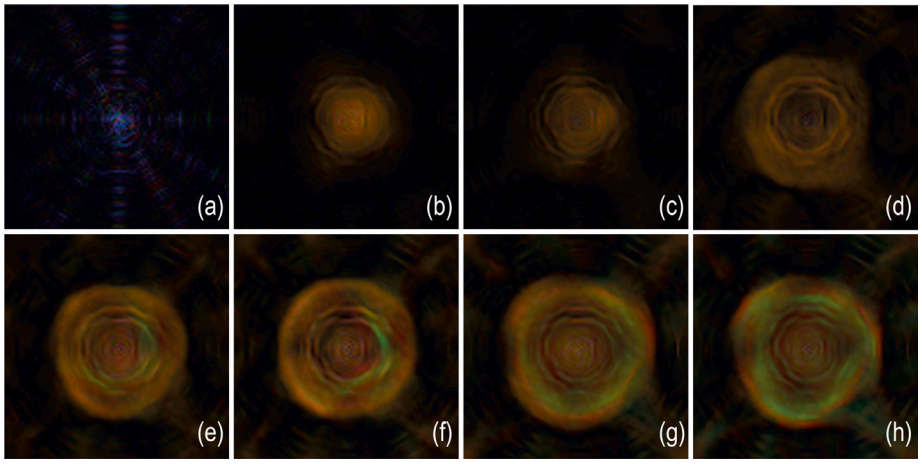

Fig. 16. Horizontal cross-sections of the reconstructed light emission density of Helium discharge 2505 at the same eight sequential time instants as Fig. 12: stable pinch (a–b), pinch instability (c–f), formation of the plasma torus around the pinch (g–h).

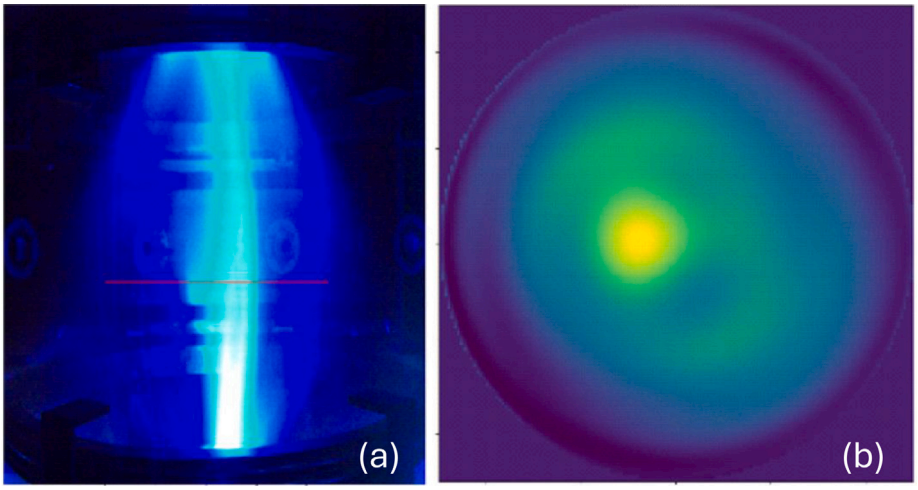

Fig. 17. Picture and related equatorial distribution of Argon plasma luminosity obtained by Zernike polynomials inversion [44].

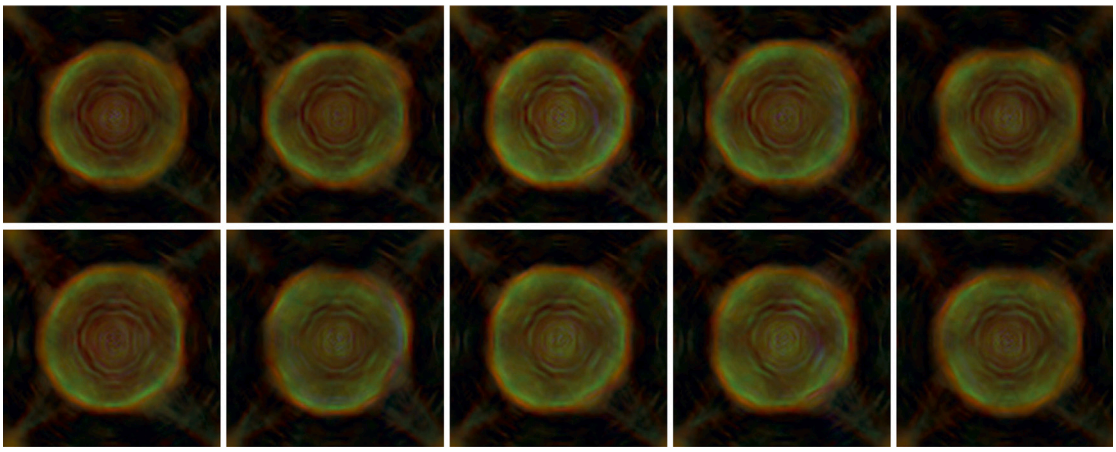

Fig. 18. Sequence of reconstructed equatorial cross-sections of light emission density of Helium discharge 2505 at 10 time instants.

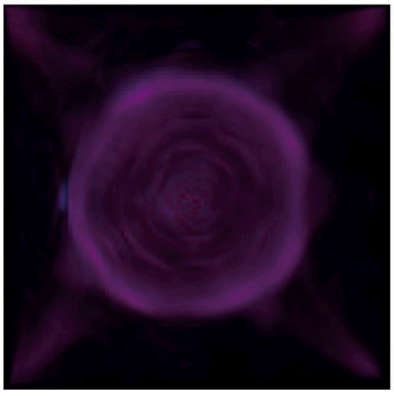

Fig. 19. Equatorial cross-section of light emission density of Hydrogen discharge 2154.

the measurement of the torus thickness, which was found to range between 0.25 and 0.35 m.

CRediT authorship contribution statement

Annamaria Pau: Writing – review & editing, Writing – original draft, Visualization, Supervision, Software, Methodology, Investigation, Formal analysis, Data curation, Conceptualization. **Shayesteh Naghinajad:** Visualization, Data curation. **Franco Alladio:** Resources, Methodology, Data curation. **Paolo Micozzi:** Resources, Methodology, Data curation. **Luca Boncagni:** Methodology, Data curation.

Declaration of competing interest

The authors declare that they have no known competing financial interests or personal relationships that could have appeared to influence the work reported in this paper.

Acknowledgments

Annamaria Pau gratefully acknowledges the funding contribution from National Center on HPC, Big Data and Quantum Computing CN00000013. This manuscript reflects only the authors' views and opinions, neither the European Union nor the European Commission can be considered responsible for them.

Data availability

Data will be made available on request.

References

[1] Johann Radon, On the determination of functions from their integral values along certain manifolds (translation from the original German text published in Berichte der Sächsischen Akademie der Wissenschaft, vol. 69, pp. 262-277, 1917), IEEE Trans. Med. Imaging MI-5 (4) (1986) 170–176.
[2] G.N. Hounsfield, Computerized transverse axial scanning (tomography): Part I. description of system, Br. J. Radiol. 46 (3) (1973) 1016–1022.
[3] A.M. Cormack, Early two-dimensional reconstruction and recent topics stemming from it, Science 209 (1980) 1482–1486.
[4] L. De Chiffre, S. Carmignato, J.-P. Kruth, R. Schmitt, A. Weckenmann, Industrial applications of computed tomography, CIRP Ann. - Manuf. Technol. 63 (2) (2014) 655–677.
[5] L. Schoeman, P. Williams, A. du Plessis, M. Manley, X-ray micro-computed tomography (μCT) for non-destructive characterisation of food microstructure, Trends Food Sci. Technol. 47 (2016) 10–24.
[6] E. Maire, P.J. Withers, Quantitative X-ray tomography, Int. Mater. Rev. 59 (1) (2014) 1–43.
[7] V. Cnudde, M.N. Boone, High-resolution X-ray computed tomography in geosciences: A review of the current technology and applications, Earth-Sci. Rev. 123 (2013) 1–17.
[8] R.S. Granetz, P. Smeulders, X-ray tomography on JET, Nucl. Fusion 28 (3) (1988) 457–476.
[9] M. Odstrcil, J. Mlynar, T. Odstrcil, B. Alper, A. Murari, Modern numerical methods for plasma tomography optimisation, Nucl. Instrum. Methods Phys. Res. Sect. A: Accel. Spectrometers Detect. Assoc. Equip. 686 (2012) 156–161.
[10] Francisco A. Matos, Diogo R. Ferreira, Pedro J. Carvalho, Deep learning for plasma tomography using the bolometer system at JET, Fusion Eng. Des. 114 (2017) 18–25.
[11] Jan Mlynar, Teddy Craciunescu, Diogo R. Ferreira, Pedro Carvalho, Ondrej Ficker, Ondrej Grover, Martin Imrisek, Jakub Svoboda, Current research into applications of tomography for fusion diagnostics, J. Fusion Energy 38 (3–4) (2019) 458–466.
[12] Avinash C. Kak, Computerized tomography with X-Ray, emission, and ultrasound sources, Proc. IEEE 67 (9) (1979) 1245–1272.
[13] P. Huthwaite, Guided wave tomography with an improved scattering model, Proc. R. Soc. A: Math. Phys. Eng. Sci. 472 (2195) (2016).
[14] Mohd Taufiq Mohd Khairi, Sallehuddin Ibrahim, Mohd Amri Md Yunus, M. Faramarzi, Goh Pei Sean, Jaysuman Pusppanathan, A. Abid, Ultrasound computed tomography for material inspection: Principles, design and applications, Meas.: J. Int. Meas. Confed. 146 (2019) 490–523.
[15] M.L.L. Wijerathne, Kenji Oguni, Muneo Hori, Tensor field tomography based on 3D photoelasticity, Mech. Mater. 34 (9) (2002) 533–545.
[16] Amir M. Alani, Francesco Soldovieri, Ilaria Catapano, Iraklis Giannakis, Gianluca Gennarelli, Livia Lantini, Giovanni Ludeno, Fabio Tosti, The use of ground penetrating radar and microwave tomography for the detection of decay and cavities in tree trunks, Remote. Sens. 11 (18) (2019).
[17] Dilber Uzun Ozsahin, Berna Uzun, Musa Sani Musa, Niyazi Şentürk, Fatih Veysel Nurçin, Ilker Ozsahin, Evaluating nuclear medicine imaging devices using fuzzy PROMETHEE method, Procedia Comput. Sci. 120 (2017) 699–705.
[18] Jeffrey Fessler, Optimization methods for magnetic resonance image reconstruction: Key models and optimization algorithms, IEEE Signal Process. Mag. 37 (1) (2020) 33–40.
[19] Yongwoo Park, Un-Chul Paek, Dug Young Kim, Characterization of a stress-applied polarization-maintaining (PM) fiberthrough photoelastic tomography, J. Lightwave Technol. 21 (4) (2003) 997–1004.

[20] Habib Ammari, Tomographic imaging with non-diffracting sources. An introduction, Math. Emerg. Biomed. Imaging 28 (10) (2008) 95–106.
[21] A.C. Kak, M. Slaney, Principles of Computerized Tomographic Imaging, IEEE Press, 1988.
[22] B Gustaffson, Mathematics for computed tomography, Phys. Scr. T61 (1996) 38–43.
[23] James Anthony Seibert, Iterative reconstruction: how it works, how to apply it, Pediatr. Radiol. 44 (3) (2014) 431–439.
[24] Wolfram Stiller, Basics of iterative reconstruction methods in computed tomography: A vendor-independent overview, Eur. J. Radiol. 109 (2018) 147–154.
[25] Richard Gordon, Robert Bender, Gabor T. Herman, Algebraic reconstruction techniques (ART) for three-dimensional electron microscopy and X-ray photography, J. Theoret. Biol. 29 (3) (1970) 471–476, IN1–IN2, 477–481.
[26] S. Donato, L. Brombal, L.M. Arana Peña, F. Arfelli, A. Contillo, P. Delogu, F. Di Lillo, V. Di Trapani, V. Fanti, R. Longo, P. Oliva, L. Rigon, L. Stori, G. Tromba, B. Golosio, Optimization of a customized simultaneous algebraic reconstruction technique algorithm for phase-contrast breast computed tomography, Phys. Med. Biol. 67 (9) (2022).
[27] Tao Zhang, Yuxiang Xing, Li Zhang, Xin Jin, Hewei Gao, Zhiqiang Chen, Stationary computed tomography with source and detector in linear symmetric geometry: Direct filtered backprojection reconstruction, Med. Phys. 47 (5) (2020) 2222–2236.
[28] Yingying Zhang-O'Connor, Jeffrey A. Fessler, Fourier-based forward and back-projectors in iterative fan-beam tomographic image reconstruction, IEEE Trans. Med. Imaging 25 (5) (2006) 582–589.
[29] David Gottlieb, Bertil Gustaffson, Patrick Forssen, On the direct Fourier method for computed tomography, IEEE Trans. Med. Imaging 19 (3) (2000) 223–232.
[30] Tugba Ozge Onur, An application of filtered back projection method for computed tomography images, Int. Rev. Appl. Sci. Eng. 12 (2) (2021) 194–200.
[31] S.R. Deans, The Radon Transform and Some of Its Applications, New York, Wiley, 1983.
[32] A. Jardin, J. Bielecki, D. Mazon, Y. Peysson, K. Król, D. Dworak, M. Scholz, Implementing an X-ray tomography method for fusion devices, Eur. Phys. J. Plus 136 (7) (2021).
[33] F. Alladio, P. Micozzi, L. Boncagni, A. Pau, S. Naghinajad, S. Macera, Y. Damizia, P. Buratti, F. Filippi, G. Galatola Teka, F. Giammanco, E. Giovannozzi, M. Iafrati, A. Lampasi, P. Marsili, PROTO-SPHERA: a magnetic confinement experiment which emulates the jet + torus astrophysical plasmas, Plasma Phys. Control. Fusion 66 (3) (2024).
[34] T. Buzug, Computed Tomography, Berlin, Heidelberg, Springer, 2008.
[35] Dominique Zosso, Benoît Le Callennec, Meritxell Bach Cuadra, Kamiar Aminian, Brigitte M. Jolles, Jean-Philippe Thiran, Bi-planar 2D-to-3D registration in fourier domain for stereoscopic X-Ray motion tracking, 6914, 2008,
[36] Xin Li, Yudong Lu, Xiaozhou Zhang, Wen Fan, Yangchun Lu, Wangsheng Pan, Quantification of macropores of Malan loess and the hydraulic significance on slope stability by X-ray computed tomography, Environ. Earth Sci. 78 (16) (2019).
[37] Mario D'Acunto, Antonio Benassi, Davide Moroni, Ovidio Salvetti, 3D image reconstruction using radon transform, Signal Image Video Process. 10 (1) (2016) 1–8.
[38] Amir Averbuch, Yoel Shkolnisky, 3D Fourier based discrete radon transform, Appl. Comput. Harmon. Anal. 15 (1) (2003) 33–69.
[39] Franco Alladio, Paolo Costa, Alessandro Mancuso, Paolo Micozzi, Stamos Papastergiou, Francois Rogier, Design of the PROTO-SPHERA experiment and of its first step (MULTI-PINCH), Nucl. Fusion 46 (2006) S613–S624.
[40] Alessandro Lampasi, Giuseppe Maffia, Franco Alladio, Luca Boncagni, Federica Causa, Edmondo Giovannozzi, Luigi Andrea Grosso, Alessandro Mancuso, Paolo Micozzi, Valerio Piergotti, Giuliano Rocchi, Alessandro Sibio, Benedetto Tilia, Vincenzo Zanza, Progress of the plasma centerpost for the PROTO-SPHERA spherical tokamak, Energies 9 (7) (2016).
[41] Paolo Micozzi, Franco Alladio, Alessandro Mancuso, Vincenzo Zanza, Gerarda Apruzzese, Francesca Bpmbarda, Luca Boncagni, Paolo Buratti, Francesco Filippi, Giuselle Galatola Teka, Francesco Giammarco, Edmondo Giovannozzi, Andrea Grosso, Matteo Iafrati, Alessandro Lampasi, Violeta Lazic, Simone Magagnino, Simone Mannori, Paolo Marsili, Paolo Piergotti, Giuliano Rocchi, Alessandro Sibio, Benedetto Tilia, Onofrio Tudisco, Final results of the first phase of the PROTO-SPHERA experiment: obtainment of the full current stable screw pinch and first evidences of the jet + torus combined plasma configurationy, Plasma Sci. Technol. 26 (2024) 025103.
[42] Pablo Luis García-Martínez, Leandro Gabriel Lampugnani, Ricardo Farengo, Effect of the helicity injection rate and the Lundquist number on spheromak sustainment, Phys. Plasmas 21 (12) (2014).
[43] A. Pau, S. Naghinajad, F. Alladio, P. Micozzi, L. Boncagni, 3D tomography of hydrogen and helium plasma produced in th PROTO-SPHERA experiment, in: Proceedings of the ASME 2024 51st Annual Review Progress in Quantitative Nondestructive Evaluation QNDE2024, Denver, Colorado, 2024, pp. 1–7.
[44] Yacopo Damizia, Matteo Iafrati, Davide Liuzza, Luca Boncagni, Paolo Micozzi, Franco Alladio, Optical tomography of the plasma on the PROTO-SPHERA experiment, Fusion Eng. Des. 169 (2021).